AIAA JOURNAL
Vol. 47, No. 9, September 2009

Optimization of Dielectric Barrier Discharge Plasma Actuators for Active Aerodynamic Flow Control

Flint O. Thomas,* Thomas C. Corke,† Muhammad Iqbal,‡ Alexey Kozlov,§ and David Schatzman¶
University of Notre Dame, Notre Dame, Indiana 46556

DOI: 10.2514/1.41588

This paper presents the results of a parametric experimental investigation aimed at optimizing the body force produced by single dielectric barrier discharge plasma actuators used for aerodynamic flow control. A primary goal of the study is the improvement of actuator authority for flow control applications at higher Reynolds number than previously possible. The study examines the effects of dielectric material and thickness, applied voltage amplitude and frequency, voltage waveform, exposed electrode geometry, covered electrode width, and multiple actuator arrays. The metric used to evaluate the performance of the actuator in each case is the measured actuator-induced thrust which is proportional to the total body force. It is demonstrated that actuators constructed with thick dielectric material of low dielectric constant produce a body force that is an order of magnitude larger than that obtained by the Kapton-based actuators used in many previous plasma flow control studies. These actuators allow operation at much higher applied voltages without the formation of discrete streamers which lead to body force saturation.

Nomenclature

b	=	electrode serration width
$\mathbf{E}$	=	electric field
$\mathbf{f}$	=	body force
Gr	=	Grashof number
h	=	electrode serration height
Re	=	Reynolds number
T	=	actuator-induced thrust
U_j	=	wall jet velocity
V_{pp}	=	peak-to-peak voltage
V_{rms}	=	root-mean-square voltage
x	=	streamwise spatial coordinate
y	=	wall-normal spatial coordinate
ε	=	dielectric constant
ρ	=	fluid density
ρ_c	=	charge density

I. Introduction

THERE is currently considerable interest in the use of single dielectric barrier discharge (SDBD) plasma actuators for aerodynamic flow control. The diverse applications are too numerous to list here but include, for example, active airfoil leading edge separation control [1,2], control of airfoil dynamic stall [3], bluff body flow control [4–8], boundary layer flow control [9–11], high-lift applications [12], and turbomachinery flow control [13–15], to name just a few. The physics surrounding the operation of SDBD plasma actuators has been the focus of several studies [16–19] and the mechanism of actuation is now fairly well understood. There have also been several efforts of varying complexity to model the influence of the actuator on the ambient fluid [20–25] for use in numerical simulations and for the development of optimum flow control strategies. For a comprehensive overview of work in the area of SDBD plasma flow control the interested reader is referred to recent comprehensive review papers [26,27].

A schematic of a SDBD plasma actuator is shown in Fig. 1. The device consists of two electrodes separated by a dielectric barrier material. In most applications the two electrodes are arranged asymmetrically and are given a slight overlap. One electrode is placed on the aerodynamic surface where it is exposed to the surrounding air (the electrode thickness in Fig. 1 is greatly exaggerated) whereas the covered electrode lies encapsulated within the dielectric material. When an ac voltage of sufficient magnitude [O (kV)] is applied between the electrodes, the dielectric barrier discharge ignites. This type of plasma discharge has the unique property that it can sustain a large volume discharge at atmospheric pressure *without arcing* because it is inherently self-limiting [17]. The formation of the plasma gives rise to an effective body force on the ambient air. Hence, the aerodynamic effect produced by plasma actuation can be represented by a body force vector $\mathbf{f}$ in the Navier-Stokes equations [27]:

$$\mathbf{f} = \rho_c \mathbf{E} \tag{1}$$

where ρ_c is the net charge density and $\mathbf{E}$ is the electric field. The body force can be tailored through the design of the electrode arrangement, which controls the spatial electric field. It is the resulting coupling of directed momentum to the surrounding air that forms the basis for flow control strategies. Although the direction of charge transfer varies during the two halves of the ac cycle that drives the actuator, the body force always has the same direction. For the electrode geometry shown in Fig. 1, air is drawn toward the wall and accelerated along the dielectric surface from the edge of the exposed electrode toward the far end of the covered electrode, thereby giving rise to a wall jet effect. The high momentum fluid near the wall has a beneficial effect in preventing flow separation in aerodynamic applications [26,27].

II. Objectives

Practical flow control applications demand robust actuators that have sufficient authority for operation in Reynolds and Mach number regimes typical of commercial and military aircraft. A primary objective of the work reported in this paper is the optimization of the SDBD plasma actuator with the goal of improving the actuator authority for application in higher Reynolds number flows than previously possible. Previous investigations have also focused on

Received 14 October 2008; revision received 26 April 2009; accepted for publication 29 April 2009.

*Professor, Department of Aerospace and Mechanical Engineering, Center for Flow Physics and Control. Associate Fellow AIAA.
†Clark Equipment Professor, Department of Aerospace and Mechanical Engineering, Center for Flow Physics and Control. Associate Fellow AIAA.
‡Postdoctoral Research Associate, Department of Aerospace and Mechanical Engineering, Center for Flow Physics and Control.
§Graduate Research Assistant, Department of Aerospace and Mechanical Engineering, Center for Flow Physics and Control.
¶Graduate Research Assistant, Department of Aerospace and Mechanical Engineering, Center for Flow Physics and Control. Member AIAA.

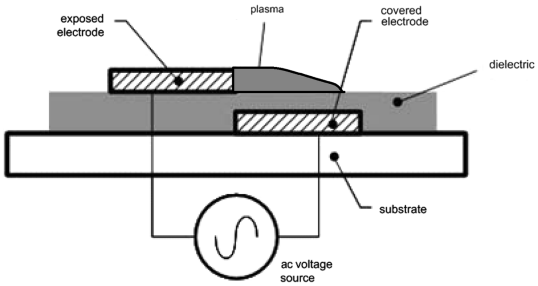

Fig. 1 Schematic of the SDBD plasma actuator.

optimization of SDBD plasma actuators for aerodynamic flow control [17,18,27–29]. However, these studies involved SDBD plasma actuators that use a thin layer (typically 1–2 mm) of Kapton polyimide film as the dielectric barrier. The work reported here builds upon these previous investigations by performing a study in which the effects of dielectric material and thickness, voltage amplitude and frequency, voltage waveform, exposed electrode geometry, and the number of actuators in series are each examined. The metric used to evaluate the performance of the actuator in each case is measured actuator-induced thrust which is proportional to the total body force.

III. Experimental Facility

The experimental facility used in this investigation consists of two primary components: 1) a plasma generation system and 2) a test cell assembly where plasma-induced momentum is measured directly as thrust on a sensitive force balance. In addition, velocity profiles of the actuator-induced flow are obtained at representative locations downstream of the edge of the exposed electrode. These components are each described in this section.

A schematic of the experimental setup for measuring the thrust produced by a plasma actuator is shown in Fig. 2. The plasma actuator is mounted on a flat surface made of a user-selected dielectric barrier material. This surface is supported vertically in a block of lightweight insulating foam material. The entire assembly is placed on a high precision electronic force balance (AND scale model GF-6100) which has a resolution of 0.098 mN (0.01 g). The plasma actuator is oriented in such a way that when an ac voltage is applied, the resulting plasma-induced flow is directed upward (away from the balance) and the reactive thrust acting downward is measured directly by the balance. The leads that power the actuator use thin wires (28AWG, 7 strands) that were not under tension and had no significant influence on the thrust measurements. The force balance had a metal case which was grounded. This, in combination with the antinoise filter shown in Fig. 3 (to be described), prevented electromagnetic noise from influencing the force measurements. This was verified by placing the balance with a fixed weight in the vicinity of the plasma actuator. The presence of plasma did not influence the weight measurement.

The entire actuator assembly and the force balance are isolated from ambient laboratory drafts by a large Plexiglas chamber with no

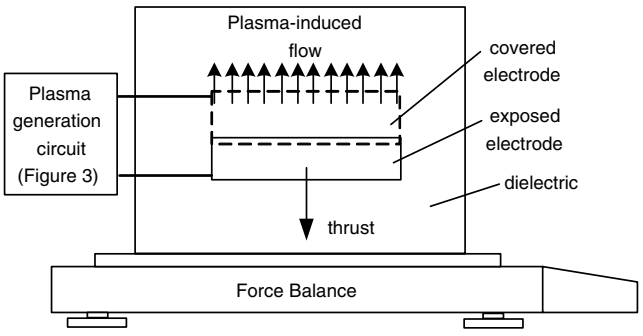

Fig. 2 Schematic of the thrust measurement facility.

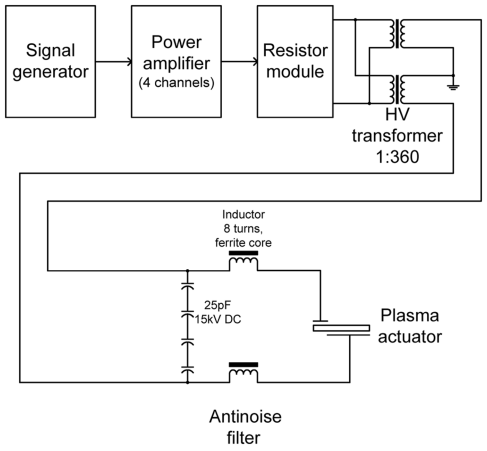

Fig. 3 Plasma generation circuit and antinoise filter.

external flow. The chamber is vented and is of sufficient size so as to prevent the actuator from inducing large-scale recirculating flow inside the chamber. The time-averaged thrust is read directly from the display of the force balance. For mean flow velocity measurements in the vicinity of the actuator, custom fabricated pitot probes made of glass are used in conjunction with a differential pressure transducer (Validyne DP103-12 pressure transducer with CD23 digital indicator/demodulator). The pressure data are acquired digitally using a personal computer and Microstar iDSC1816 A/D board. Alternately, the velocity induced by the actuators was measured using two-component particle image velocimetry (PIV). In this case the air was seeded using olive oil droplets of nominally 1 μm diameter produced by a TSI, Inc. atomizer. The charge on the droplets resulting from their shear-dominated formation in the atomizer is, at most, a few hundred electrons. Dimensional reasoning shows that even for the maximum electric field encountered in the experiments the aerodynamic force on the droplets dominates. A model Y120-15 New Wave Research Nd:Yag laser system produced double pulses with a 25 μs interval at a maximum repetition rate of 15 Hz. PIV images were captured by a PIV CAM 10–30 digital camera. TSI, Inc. Insight 6 software was used to process the image pairs and compute the time-averaged velocity fields.

Copper tape of 0.04 mm thickness was used to form each actuator electrode. The exposed electrode was mounted directly on the dielectric surface. In each case the overlap between the exposed and covered electrode was set to one-half of the dielectric thickness (which was varied in the investigation). Unless otherwise noted, the width of both the exposed and covered electrodes was kept constant at 2.54 and 5.08 cm, respectively. The length of both electrodes was either 10.16 or 20.32 cm, depending on the particular experiment. The upstream edge of the exposed electrode was covered with three layers of 0.051-mm thick Kapton polyimide film to avoid the formation of plasma at that edge. The covered electrode was insulated with two layers of 0.762-mm thick high-voltage tape (3M Scotch 130C).

The second major component of the setup is the circuit that is used to create the high-frequency, high-amplitude ac voltage required for the plasma actuator. This is shown schematically in Fig. 3. A low amplitude signal from an arbitrary waveform function generator (e.g., Agilent Technologies model 33220A) is first supplied to twin two-channel power amplifiers (Crown XTi4000). The amplified voltage from each of the four channels is then fed through a resistor module containing four 2 Ω, 300 W ballast resistors which are connected together at the primary coils of two custom-made transformers (Corona Magnetics) of winding ratio 1:360 and maximum output voltage 25 kV ac with a current of 70 mA. The primary coils of the transformers are connected in parallel but in the opposite polarity. The low potential output of the secondary coils is connected to ground. High voltage used by the plasma actuator is taken from the two high potential leads of the transformers giving the same signal in the opposite polarity so that the effective winding ratio of this system is 1:720.

The voltage applied to the actuator is measured by a LeCroy PE20kV dc frequency compensated high-voltage probe. The current through the actuator is measured by two Pearson Electronics model 2100 current meters. The current meters are installed on both high-voltage wires near the plasma actuator to exclude the additional current due to the corona discharge around relatively long high-voltage wires. The signals from these devices are processed in real time by a LeCroy LT262 oscilloscope, which calculates the ac power dissipation by point-by-point integration of the instantaneous product of voltage and current over the course of many full ac cycles.

Dielectric barrier discharge is accompanied by high intensity radio frequency electromagnetic noise. A custom designed antinoise filter is used to suppress this noise. The filter, which is shown in Fig. 3, is installed on the plastic foam base near the actuator. In essence, it is a low-pass filter consisting of two inductors (8 turns, ferrite core, 31.1 mm outer diameter, 19.1 mm inner diameter, 15.9 mm ferrite cylinder height) and a battery of four high-voltage capacitors (25 pF, 15 kV dc maximum). The filter does not affect the 1–10 kHz actuating frequency but prevents high-frequency noise from entering the high-voltage wires which feed the plasma actuators.

IV. Experimental Results

In this section experimental results from the parametric study aimed at the maximization of measured actuator thrust are presented. Consideration is first given to the influence of dielectric material and thickness on the actuator thrust.

A. Effect of Dielectric Material and Thickness

Three layers of 0.051-mm thick Kapton polyimide film have often been used as a dielectric barrier in SDBD plasma actuators used for flow control [3,17]. Therefore, thrust measurements using 0.15 mm Kapton as the dielectric will be considered a baseline case against which actuators using other dielectric materials will be compared. The thrust per unit span measured for the plasma actuator using 0.15-mm Kapton dielectric is presented in Fig. 4. In this figure the measured actuator thrust per unit span is plotted as a function of the applied rms ac voltage. The ac frequency used for the Kapton-based actuator is 4.4 kHz which is similar to that used in many previous flow control studies. As indicated in Fig. 4, the maximum measured thrust per unit span was about 0.022 N/m. Unless otherwise noted, measured values are stated at $\pm 3\%$ relative uncertainty at the 95% confidence interval. This relative uncertainty was computed using standard error propagation methods as described in [30]. The maximum achievable voltage for this baseline case was approximately 5 kV_{rms} or 17 kV_{pp} (a positive sawtooth waveform was used). For higher applied voltages, filamentary structures (streamers) were observed to develop in the plasma. Once streamer formation occurred, further increases in applied voltage did not result in a significant increase in thrust but did significantly increase the dissipated power. Since the onset of streamer formation is associated with maximum thrust and increased power dissipation, this will be referred to as the actuator's "saturation condition." It becomes apparent that to achieve increased actuator authority it is necessary to operate the actuators at higher ac voltages without incurring the onset of streamer formation.

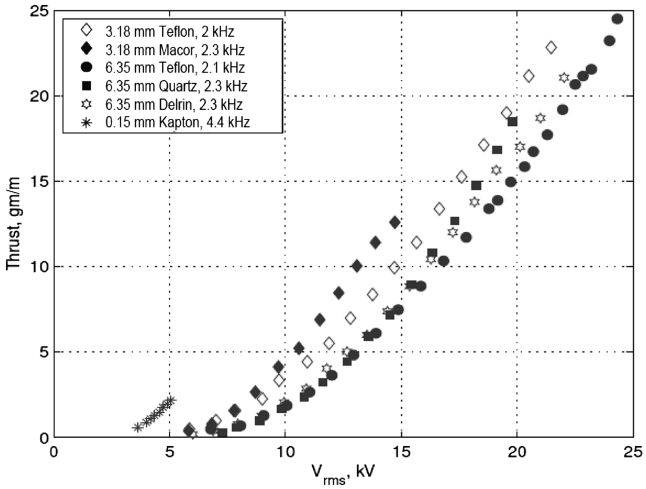

Fig. 4 Measured thrust per unit span/g versus rms applied voltage for various dielectric materials.

In an effort to increase the maximum achievable thrust, dielectric barrier materials with a high dielectric strength and dielectric constant comparable to Kapton ($\varepsilon = 3.9$) but of greater thickness were tried. In particular, experiments were performed with actuators using quartz, Teflon, Delrin, and Macor ceramic (with dielectric constants of $\varepsilon = 4.3$, 2.0, 3.7, and 6.0, respectively). Figure 4 also shows the measured thrust curves for actuators using these dielectric materials. In each case the ac frequency was optimized for the actuator and is provided in the legend. The effect of frequency will be discussed later in Sec. IV.B. As was the case for the Kapton actuator, the thrust curves terminate at the ac voltage associated with the onset of saturation. It is apparent from this figure that the use of these dielectric materials at the indicated thicknesses results in a very significant increase in body force. For example, in the case of the quartz dielectric with thickness of 6.35 mm, maximum thrust now corresponds to 0.18 N/m at a voltage of 20 kV_{rms} (68 kV_{pp}). Hence, by changing the dielectric material and thickness, the body force has increased by a factor of approximately 8.2 over that exhibited by the Kapton actuator. Thrust curves for actuators using Teflon (which has the lowest dielectric constant of any of the materials tested) with thicknesses of both 3.18 and 6.35 mm are shown in Fig. 4. Note that the Teflon-based actuator with the thicker dielectric achieves higher saturation voltage and saturation thrust. In fact, by using 6.35 mm Teflon as the dielectric *an order-of-magnitude improvement in body force over Kapton-based plasma actuators is achieved.* The primary reason for the increased body force shown in Fig. 4 is the substantial increase in thickness of the dielectric barrier used in each case. This allows for greater applied voltages without the occurrence of saturation. It is also noted that for a given voltage below saturation, the 3.18-mm Teflon actuator produces a larger body force than the 6.35-mm Teflon actuator.

For each of the actuators shown in Fig. 4, the variation of actuator thrust with rms applied voltage appears to follow a power law. This is confirmed in Fig. 5 which presents the thrust for the 6.35-mm-thick Teflon-based actuator as a function of applied rms voltage in logarithmic coordinates. This figure clearly shows that the actuator thrust initially exhibits a power law variation with applied voltage as $T \propto V_{rms}^{3.5}$. This result was consistent for all actuator combinations examined. Note, however, that Fig. 5 also shows that at the highest voltages, $T \propto V_{rms}^{2.3}$. Reduced thrust response of the actuator at the higher voltages is likely a precursor to actuator saturation. It is *not* due to the limited size of the covered electrode (which can have the effect of constraining the spatial extent of the plasma forming region at highest voltage) because plasma never reached the end of the covered electrode in these experiments. More significantly, however, Fig. 5 shows that the thrust variation with applied voltage is always greater than quadratic. Although it is desirable to have a simple physical explanation for the two-third power law scaling behavior shown in Fig. 5, the authors are unaware of any current theoretical model that will yield such scaling. Only the lumped element model [25] which accounts for the time-dependent plasma formation has reproduced this scaling behavior.

Dielectric materials to be used in SDBD plasma actuator applications must possess a high dielectric strength and must not chemically degrade in the presence of the plasma. In addition, lumped element actuator simulations reported in [25] suggest that using a dielectric material of lower dielectric constant can significantly increase the maximum achievable voltage before onset of saturation. A lower dielectric constant reduces the effective capacitance of the actuator and thereby also reduces the local concentration of electric field lines. This has the equivalent effect of lowering the current density which should allow operation of the actuator at higher voltage without giving rise to streamer formation.

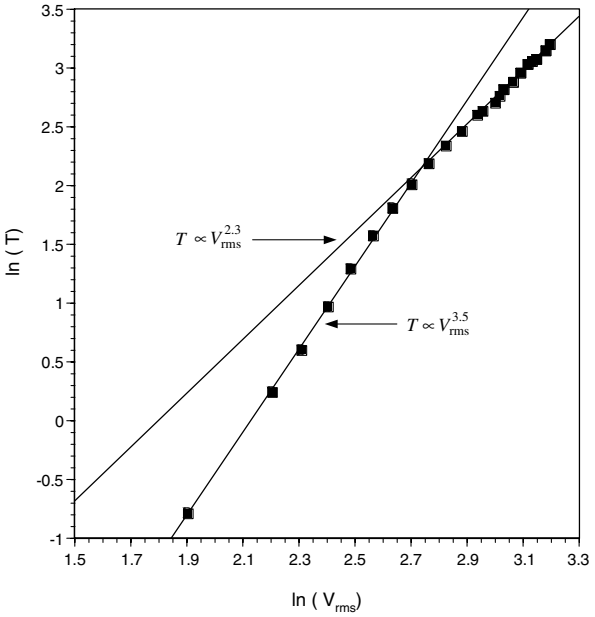

Fig. 5 Thrust curve for the 6.35-mm Teflon actuator in logarithmic coordinates.

The importance of selecting a suitable dielectric material for the plasma actuator is highlighted in Fig. 6 which presents the measured saturation thrust for different plasma actuators as a function of the dielectric constant. For these experiments, the dielectric thickness was 6.35 mm in each case and the operating frequencies were very similar. Higher saturation thrust is clearly associated with lower dielectric constant. This is due to the fact that materials with lower dielectric constant allow higher voltages to be applied before the onset of streamer formation.

B. Effect of ac Frequency

In this section the effect of the applied ac frequency on the maximum saturation voltage (and thrust) produced by the actuator is examined. For these experiments an actuator using 6.35-mm-thick quartz as the dielectric barrier was used.

Figure 7 presents the measured actuator thrust per unit span as a function of actuator peak-to-peak voltage for a range of actuation frequencies. A sinusoidal waveform was used for most of the experiments since it exhibits the smallest distortion due to the capacitance and inductance in the plasma actuator circuit compared to other waveforms. However, for the 2 kHz case, results for both sinusoidal and positive sawtooth waveforms are presented. The voltage was measured at the transformer output so the results for the thrust did not depend on whether or not the system was at resonant frequency. Further, power losses at the transformer are small since the operating frequency is high (1–8 kHz). These losses do not significantly affect the power measurements.

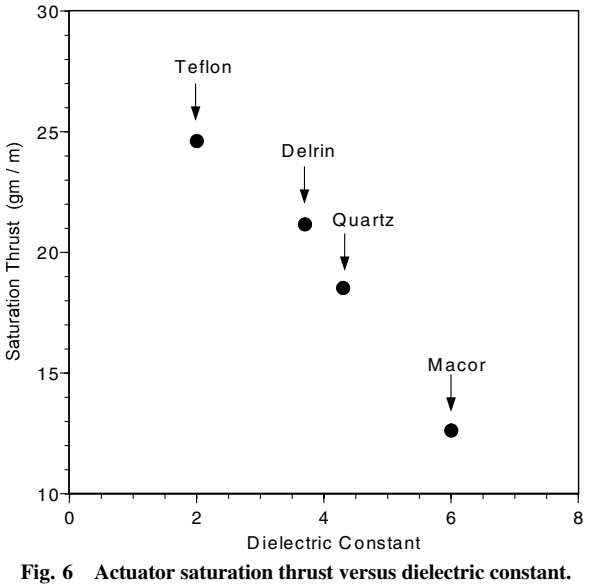

Fig. 6 Actuator saturation thrust versus dielectric constant.

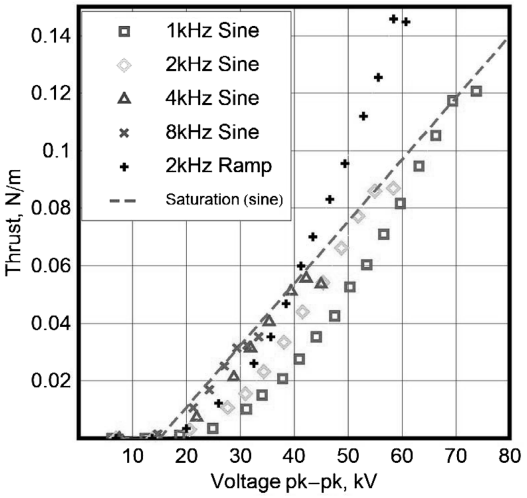

Fig. 7 Actuator thrust as a function of applied voltage for different frequencies (6.35-mm thick quartz).

For the sinusoidal waveform, the saturation thrust corresponding to the onset of saturation is apparent at each selected frequency. A dashed curve connecting the saturation thrust at each frequency for the sinusoidal waveform is shown in Fig. 7 and exhibits an approximately linear variation with applied peak-to-peak voltage. *It is clear from Fig. 7 that increased saturation thrust is associated with operation of the actuator at lower ac frequencies*. For the 2 kHz case, the saturation thrust reached by the actuator with a positive ramp waveform is nearly twice as high as with a sinusoidal waveform at the same frequency. This is consistent with previous actuator optimization studies which have shown the benefit of a positive sawtooth waveform over both sinusoidal and negative sawtooth waves [17,18]. These references have shown that the positive sawtooth prolongs that portion of the ac cycle during which electrons are transferred from the exposed electrode to the dielectric surface (the so-called forward stroke [17]) and minimizes that portion in which electrons are transferred back to the exposed electrode from the dielectric surface (the backward stroke).

Figure 7 also shows that for ac voltages below saturation, a given actuator thrust may be obtained at a lower applied voltage by operating the actuator at a higher ac frequency. For example, a thrust of 0.05 N/m is achieved at 50 kV_{pp} at a frequency of 1 kHz but only 39 kV_{pp} is required at 4 kHz. It may also be noted from Fig. 7 that the positive ramp waveform requires a lower voltage to achieve a given thrust than the sinusoidal waveform at the same frequency.

Figure 8 contrasts the visual appearance of the plasma actuator when operating below saturation (shown in 8a.) with its appearance at saturation thrust for those frequencies considered previously in Fig. 7. Sinusoidal ac excitation has been used in each case. Figure 8 clearly shows that both the number and the brightness of discrete streamer filaments increase with the applied ac frequency. This, in combination with the saturation thrust measurements shown in Fig. 7, clearly shows that streamer formation serves to limit the maximum thrust that can be produced by the actuator. Once the streamers form, further increases in applied voltage give rise to increased power dissipation in the actuator without significant improvement in saturation thrust. This aspect is clearly shown in Fig. 9 which presents the same thrust data presented earlier in Fig. 7 but as a function of the dissipated power.

The results shown in Figs. 7–9 are for a quartz dielectric thickness of 6.35 mm. To investigate the generality of the trends observed, experiments were repeated for quartz dielectric thicknesses of 3.81 and 1.59 mm. The results of these experiments are summarized in

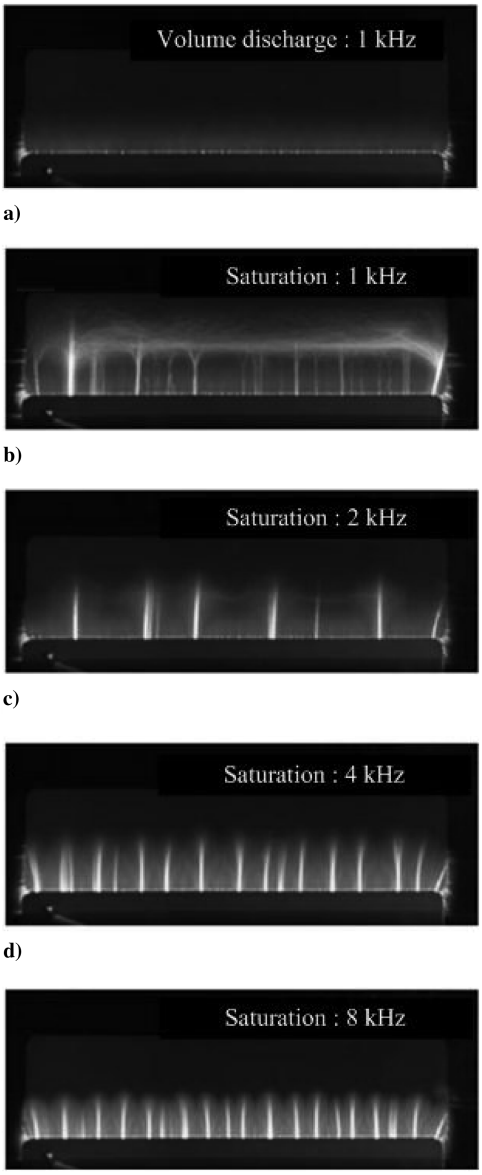

Fig. 8 Filamentary structure of plasma discharge at the saturation thrust condition for various frequencies (6.35-mm quartz dielectric): a) 1-kHz, typical nonsaturated volume discharge; b) saturation at 1 kHz; c) saturation at 2 kHz; d) saturation at 4 kHz; e) saturation at 8 kHz.

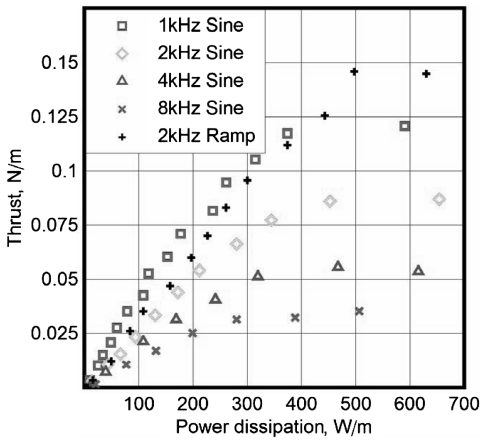

Fig. 9 Actuator thrust as a function of dissipated power for different frequencies (6.35-mm thick quartz).

Fig. 10. Figure 10a presents the measured saturation thrust as a function of peak-to-peak saturation voltage. Different values of saturation thrust for a given dielectric thickness were obtained by varying the ac frequency. This figure shows that regardless of the dielectric thickness, the saturation thrust, and hence body force, varies linearly with saturation voltage. A thicker dielectric allows one to use larger peak-to-peak voltage and thereby attain larger body force. Figure 10b presents the measured saturation thrust as a function of ac frequency and confirms that in each case maximum body force is associated with low frequency operation of the actuator.

C. Effect of Multiple Actuators in Series and Covered Electrode Width

Further enhancements in body force can be achieved by using multiple actuators in series. To demonstrate this idea, experiments were performed with actuator arrays that contained up to three actuators in series. The geometry used for the multiple actuator arrangement is shown schematically in Fig. 11. In each case, the width of the exposed electrodes was 12.7 mm. The width of the covered electrode was varied between 12.7 and 50.8 mm. Both electrodes extend 101.6 mm in the spanwise direction. The spacing between the downstream edge of the covered electrode and the upstream edge of the exposed electrode immediately downstream was kept constant at 12.7 mm. The dielectric material was Teflon of 6.35 mm thickness.

Figure 12 presents the measured thrust per unit span for single, twin, and three actuator configurations versus applied rms voltage (V_{rms}). The solid symbols present results for actuators using a covered electrode of 25.4 mm width. The open symbols present corresponding results for $w = 50.8$ mm covered electrode. In both cases there is clearly a benefit in using multiple actuators since it increases the measured thrust over that produced by the single actuator at the same voltage. However, the thrust does not simply linearly sum with the number of actuators. Based upon the measurements shown in Figs. 12, Fig. 13 presents the variation with applied rms voltage of the ratio of thrust produced by dual and triple actuator arrays to that of the single actuator. The ratio exhibits a fairly weak variation with applied voltage with lower values occurring at the highest voltage. The improved thrust performance for the case of $w = 50.8$ mm shows that it is important in both single and multiple actuator arrangements to have sufficient width of a covered electrode so as not to constrain the spatial extent of the plasma forming region at the highest applied voltages. In general, Fig. 13 shows that $T_{2\text{act}}/T_{1\text{act}} > 1.5$ and $T_{3\text{act}}/T_{1\text{act}} > 2$ for both cases. It is conjectured that the thrust does not linearly sum in a multiple actuator arrangement due to the interaction between the applied electric field associated with each actuator. That is, the local electric field is globally determined. Proof of this, however, would require varying the distance between the actuators. This remained fixed in the experiments reported here.

The effect of the width w of the covered electrode on the thrust produced by single and multiple actuator arrays was more fully investigated by systematically varying w over the range $1.27\ \text{cm} \leq w \leq 5.08\ \text{cm}$. For these experiments the spacing between the actuators was held constant at 12.7 mm. Results for an applied voltage of $V_{\text{rms}} = 20$ kV are presented in Fig. 14 and these may be considered representative of experiments performed at other applied voltages. In each case, it can be seen that the thrust (body force) is reduced at fixed voltage if the width of the covered electrode constrains the plasma forming region. For large electrode width, Fig. 14 shows that there is a saturation effect indicating that covered electrode width beyond that necessary to encompass the region of plasma formation does not provide additional thrust benefit.

D. Measurement of the Actuator-Induced Flow

To investigate the nature of the flow induced by the steady operation of both single and multiple actuator arrays, velocity measurements were made using two methods: by using nonintrusive PIV and by wall-normal traverses with a glass pitot probe at selected locations downstream of the actuator. Figure 15 presents a sample PIV measurement of the time-averaged flow induced by a single

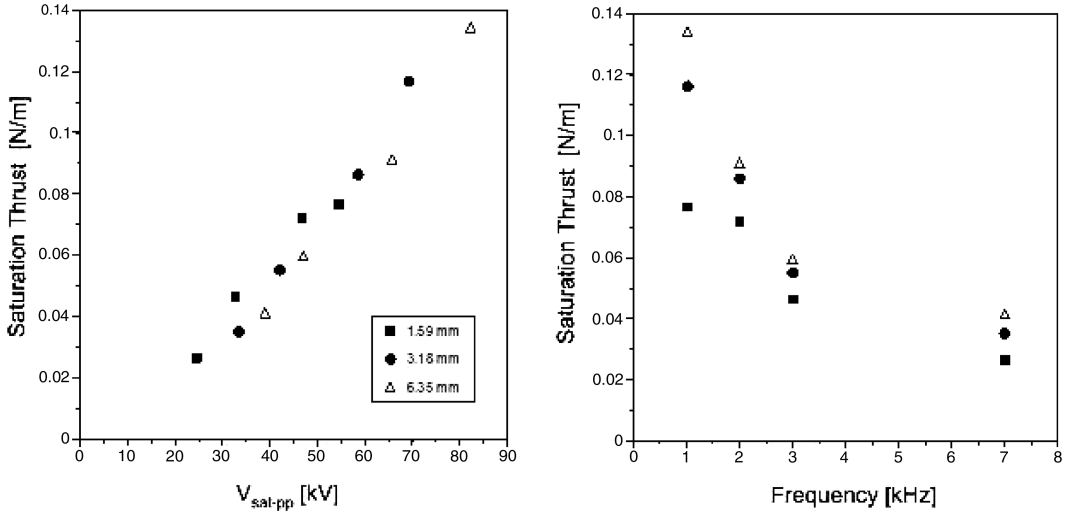

a) b)

Fig. 10 Maximum measured thrust for different quartz dielectric thicknesses as function of a) peak-to-peak saturation voltage; b) ac frequency.

plasma actuator. This figure serves to indicate the essential aspects of the actuator-induced flow. The locations and extent of both the exposed and covered electrodes are indicated in the figure. The measurement plane is located in the center plane of the electrode's 38.1 cm span. The dielectric is 3.18-mm-thick Teflon and the ac voltage is a positive sawtooth of 40 kV peak-to-peak with a 2 kHz carrier. Figure 15 clearly shows how the actuator gives rise to a body force that draws ambient air toward the wall. This, in combination with the impermeability condition at the wall, gives rise to a wall jet that forms downstream of the actuator. A sample wall-normal mean velocity profile derived from the PIV was obtained 78 mm downstream of the covered electrode and is also presented in Fig. 15.

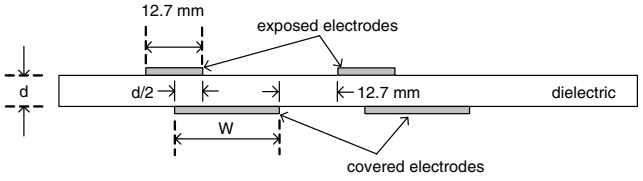

Fig. 11 Schematic of the geometry used to measure thrust from multiple actuators.

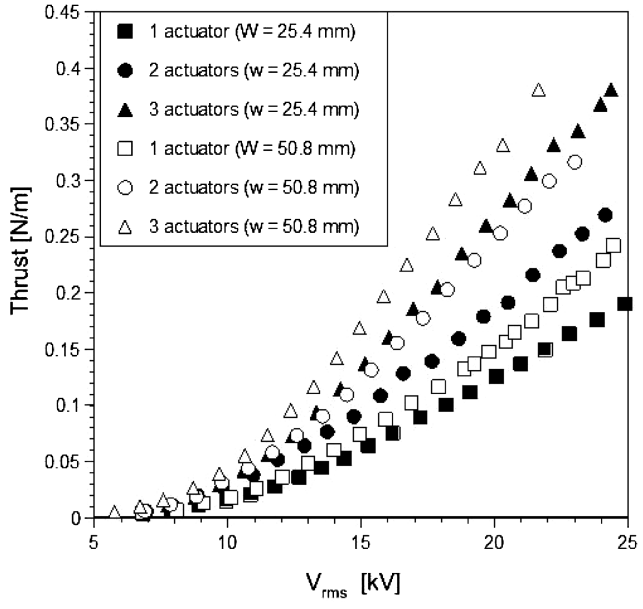

Fig. 12 Measured thrust for multiple actuator configurations.

It clearly shows the development of a wall jet emanating from the actuator. The maximum velocity indicated is approximately 1.8 m/s, but it should be noted that this value is limited by the spatial resolution of the PIV measurement which does not allow measurement sufficiently close to the wall to resolve the near-wall peak.

Actuator-induced velocity measurements were also performed by wall-normal traverses of a glass pitot tube (built in-house) of outer diameter of 0.76 mm and inner diameter of approximately 0.25 mm. The relative uncertainty of the velocity measurements is $\pm 4\%$ (at 95% confidence). Measurements were performed for the case of a single actuator as well as for dual and triple actuator arrays with geometry identical to that shown previously in Fig. 11. In each case, the wall-normal traverses were performed at several locations downstream of the actuator. Figures 16a and 16b present representative mean velocity profiles obtained at locations 3.81 and 5.08 cm downstream of the last exposed electrode, respectively. These exhibit a wall jet profile shape with peak velocity occurring approximately 1.4 mm above the wall. For these measurements the actuators were operated at $V_{\text{rms}} = 17$ kV and used 6.35-mm Teflon dielectric. The covered electrode was 2.54 cm wide. The span of the electrodes was 101.6 cm.

Figure 16 shows that as the number of actuators increases, the profiles exhibit a modest increase in the near-wall peak velocity, but more significantly, a substantial thickening of the wall jet occurs. The pitot-tube velocities shown in Fig. 16 are based on an assumed value of fluid density ρ corresponding to ambient laboratory conditions. Numerical integration of measured velocity profiles such as those in Fig. 16 showed that the integrated flux $\int_0^\infty U_j^2\,dy$ is nearly constant within experimental uncertainty (where U_j is the actuator-induced velocity, y is the wall-normal coordinate). As an example, for the profiles shown in Fig. 16 the disparity between integrated flux at the two indicated streamwise locations is 2, 3, and 5.7% for the 1, 2, and 3 actuator cases, respectively.

For both single and multiple actuator cases, the thrust calculated from integrated momentum flux was always found to be greater than that by direct thrust measurement (e.g., Fig. 12). The disparity was 3.3, 15.7, and 12.4% for the 1, 2, and 3 actuator cases, respectively. One would expect the thrust calculated from the integrated wall jet momentum flux to be higher because it assumes fully two-dimensional flow and neglects end effects which are, no doubt, present. It is also possible that the difference is due to the actual density of the actuator-induced near-wall flow. Equating the integrated momentum flux to the direct measurement of thrust for both the two and three actuator configuration cases allows an estimate of the wall jet fluid density (and hence temperature). This shows that the appropriate density would be approximately 1.08 kg/m^3 (as opposed to the assumed density of 1.2 kg/m^3) for which the corresponding wall jet fluid temperature would be approximately 327 K (54 °C), certainly

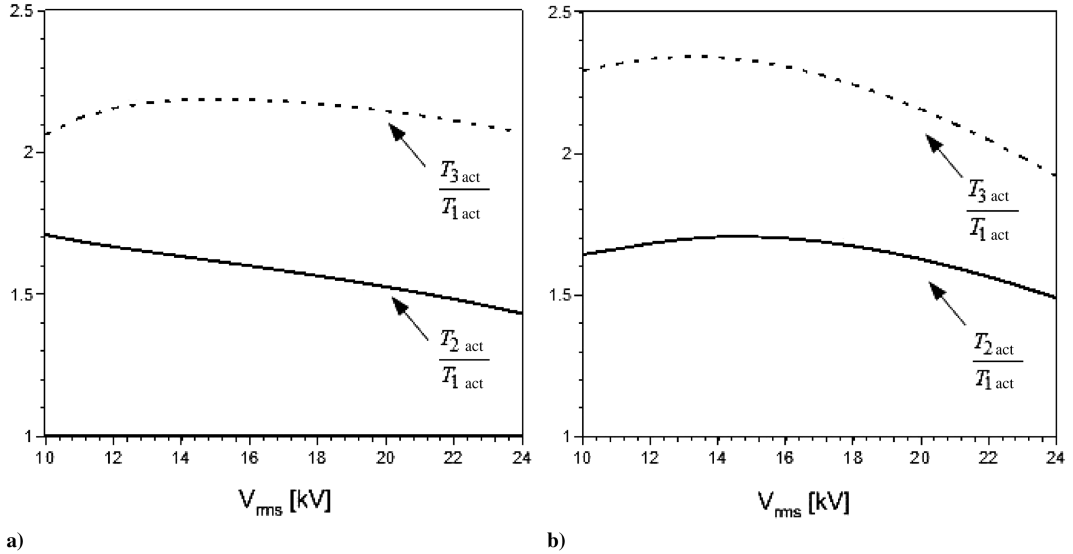

Fig. 13 Thrust ratios T_{2act}/T_{1act} and T_{3act}/T_{1act} versus applied rms voltage; a) 25.4-mm covered electrodes; b) 50.8-mm covered electrodes.

plausible for a cold, weakly ionized SDBD plasma. This value has not, however, been confirmed by independent measurement. If this is indeed the case, then the velocities shown in Fig. 16 need to be increased by a factor of approximately $\sqrt{\rho_{\text{STP}}/\rho_{\text{actual}}} = 1.07$. It is also of interest to note that at this inferred fluid temperature the ratio of buoyancy to inertial forces as measured by the ratio of the Grashof number to the square of the Reynolds number $Gr/Re^2 \approx 1.7 \times 10^{-3}$, so that inertia forces dominate and buoyancy forces are essentially negligible in the operation of the actuators.

Figure 17 presents sample actuator velocity profiles in similarity coordinates, $U_j/U_{j\max}$ versus y/δ, where $U_{j\max}$ is the local maximum actuator-induced velocity and δ is a local length scale corresponding to the wall-normal distance where $U_j = 0.5U_{j\max}$. Figure 17 shows that the measured mean velocity profiles exhibit self-similarity to very good approximation and that the normalized profile shape is largely independent of distance from the last exposed electrode. This is true irrespective of the number of actuators used in the array.

E. Effect of Electrode Geometry

The results presented previously are based on experiments with actuators that use exposed electrodes that have straight edges. In this section measurements are presented in which the downstream edge of the exposed electrode is serrated. Because the edge of the electrode represents an isopotential surface, it follows that a serrated electrode provides a means of locally increasing the applied electric field. This, in turn, is expected to have a favorable effect on the body force produced by the actuator. The geometry of the electrode serration is a triangular pattern characterized by the height h and width b of each serration. Actuators using serrations with several different combinations of b and h were constructed and the actuator-induced thrust per unit span measured as a function of applied voltage. For these experiments the actuators used 3.18-mm-thick quartz dielectric. The covered electrode width was fixed at 101.6 mm while the span of both electrodes was 203.2 mm. A positive sawtooth waveform at a frequency of 1 kHz was used. Based upon these experiments it was determined that for an exposed electrode of 2.54 cm width, a triangular serration with $b = 3.18$ mm and $h = 12.7$ mm ($b/h = 4$) was

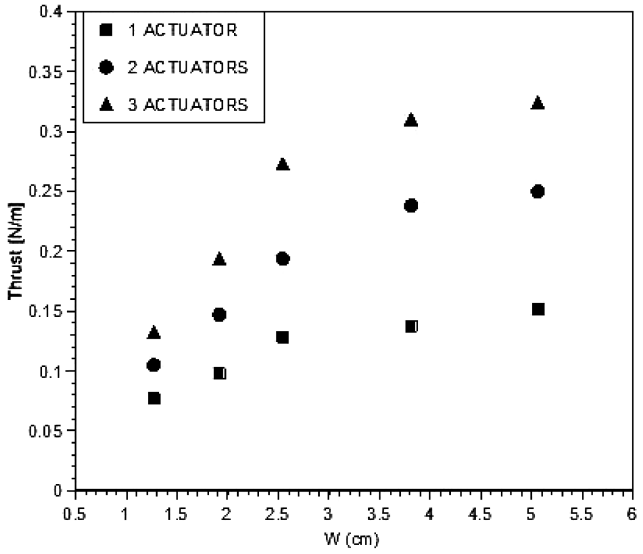

Fig. 14 Effect of covered electrode width w on single and multiple actuator thrust ($V_{\text{rms}} = 20$ kV).

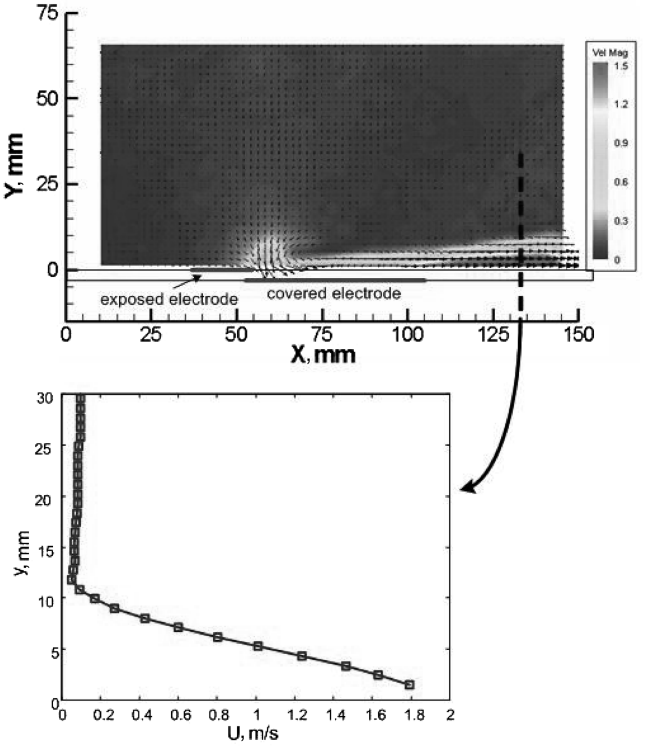

Fig. 15 PIV time-averaged velocity field for a single plasma actuator ($V_{\text{pp}} = 40$ kV).

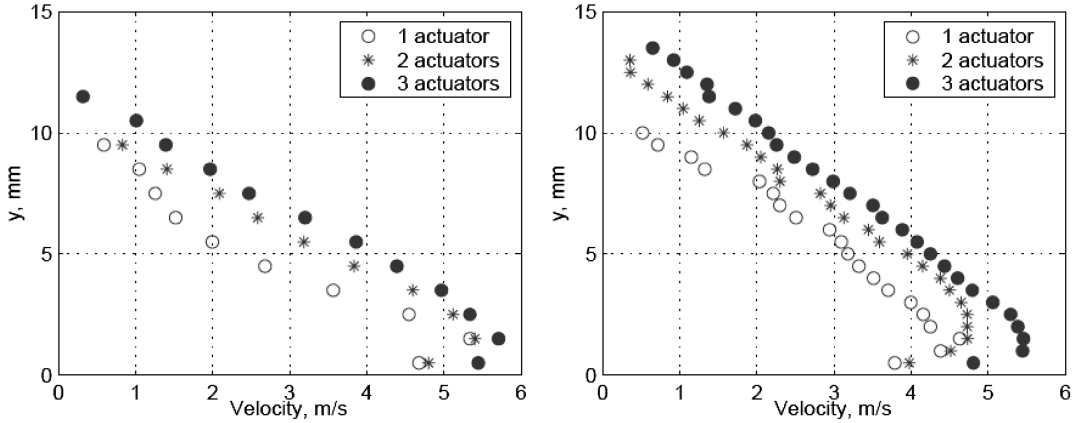

Fig. 16 Mean velocity profiles for single, dual, and triple actuator configurations: a) 3.81 cm downstream; b) 5.08 cm downstream.

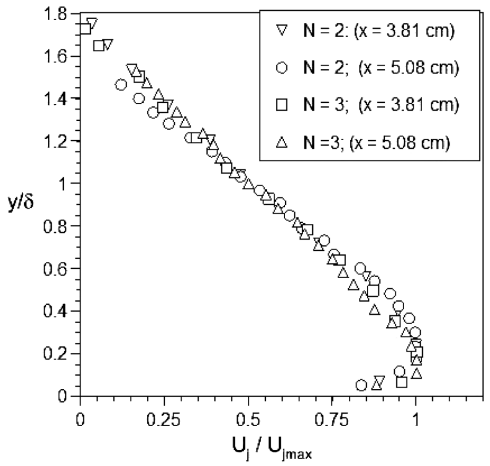

Fig. 17 Actuator mean velocity profiles in similarity scaling.

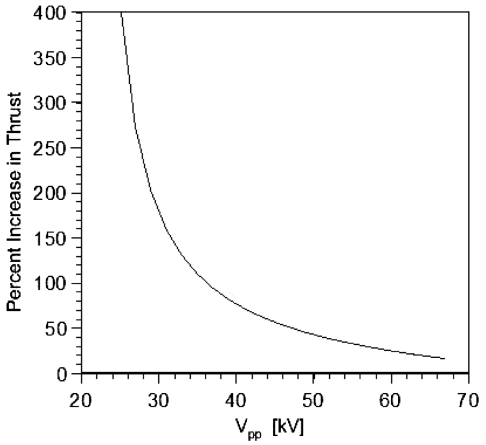

Fig. 19 Percentage thrust improvement for the actuator with a serrated electrode.

optimum in terms of measured thrust. Figure 18 compares the measured thrust per unit span as a function of applied ac peak-to-peak voltage for actuators with straight and optimized serrated edge. This figure clearly shows the benefit of using a serrated exposed electrode. For a given applied voltage, the actuator with the serrated electrode provides a significant increase in thrust over that produced by the actuator with straight electrode. Although the serrated electrode data presented in Fig. 18 are for the optimum case, actuators using triangular serrations of various b and h combinations also exhibited significant thrust benefit over the straight electrode geometry.

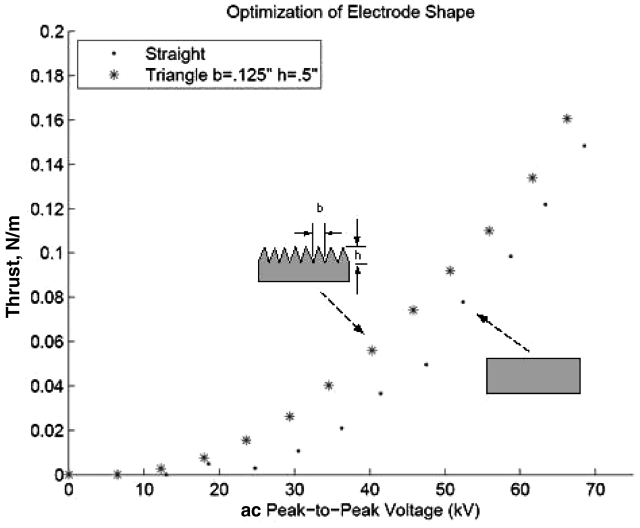

Fig. 18 Thrust per unit span for actuators with straight and optimum serrated electrodes.

Figure 19 presents the percent increase in thrust associated with the use of the optimum serrated electrode geometry as a function of peak-to-peak voltage. This figure is based on a comparison of least-squares fits to the thrust data shown in Fig. 18. For the optimum serration, the effective increase in span of the exposed electrode is 5%. Figure 19 shows that the percent increase in thrust due to the serration far exceeds this. The very large thrust gain at the lower applied voltages is a consequence of the fact that the plasma initiates earlier for the serrated electrode due to the higher local electric field. It is significant to note that for typical actuator operating voltages (say, in the 40–50 kV_{pp} range), the thrust improvement is greater than 50%. The thrust gain is clearly diminished at the highest operating voltages. This is due to the fact that for the straight electrode $T \propto V^{3.5}$, whereas for the serrated electrode the experiments show that $T \propto V^{2.3}$. As a consequence, the experiments also showed that the saturation thrust of the actuator with serrated electrode was similar to that with the straight electrode.

V. Conclusions

Based upon the experimental results obtained in the parametric study presented in this paper the following conclusions are drawn:

1) The maximum body force produced by a SDBD plasma actuator is limited by the formation of streamers in the plasma. Once they form, increasing the applied voltage serves only to increase the power dissipation without significantly increasing the body force. One key to achieving higher actuation authority is to delay streamer

formation in the plasma. By using dielectric barrier materials with high dielectric strength, low dielectric constant, and increased thickness, an order-of-magnitude gain in body force over the commonly used 6-mil-thick Kapton actuators is demonstrated. The use of thicker dielectric materials with low dielectric constant serves to spread the electric field lines on the dielectric barrier surface which lowers the current density and thereby impedes streamer formation.

2) For a given actuator, higher saturation body force is obtained by lowering the applied ac frequency. In fact, it is found that saturation body force varies linearly with applied voltage as ac frequency is reduced. This result is consistent with images of the actuator at saturation which show that the number of discrete streamers is proportional to the ac frequency. In contrast, for operation of the actuator at voltages below the saturation condition, high-frequency operation of the actuator allows a given body force to be achieved at considerably lower applied voltage.

3) For low to moderate operating voltages, the body force is found to follow a power law and is proportional to the applied voltage to the 3.5 power. At higher voltages approaching saturation, the body force is proportional to the applied voltage to approximately the 2.3 power. This better-than-quadratic scaling of the body force with applied voltage is a characteristic which viable plasma actuator models should be able to duplicate.

4) SDBD plasma actuators using an exposed electrode with the downstream edge serrated provide a considerable increase in body force over that produced by the same actuator with a conventional straight-edge electrode. For an exposed electrode of 2.54 cm width, triangular serrations with height of 12.7 mm and width of 3.18 mm proved optimum. The benefit is a strong function of applied voltage with greatest benefit at low voltages. This is because plasma ignition occurs earlier (i.e., at lower voltage) with the serrated electrode. However, even at typical operating voltages the thrust gain is nominally 50–60%. At the highest voltage the benefit of the serrated electrode is diminished since $T_{\text{serrated}} \propto V^{2.3}$ whereas, $T_{\text{straight}} \propto V^{3.5}$. The serrated electrode has little influence on the saturation voltage.

5) For both the single actuator and the multiple actuator arrays, achieving optimum body force requires that the covered electrode width is sufficient that the plasma forming region is not artificially constrained at the highest applied voltages. In the parametric experiments reported in this paper, a covered electrode width of approximately 50.8 mm was sufficient for applied rms voltages up to 25 kV. The need for sufficient covered electrode width, of course, imposes a spacing constraint on the placement of multiple actuators in arrays on subscale aerodynamic models in flow control experiments.

6) For multiple actuator arrays, the total body force increases with the number of actuators but does not sum linearly. Thrust ratios for multiple and single actuators exhibit a weak variation with applied voltage as shown in Fig. 13. However, it was found that in general, $T_{2\text{act}}/T_{1\text{act}} > 1.5$ and $T_{3\text{act}}/T_{1\text{act}} > 2$.

7) Velocity measurements of the flow induced by the actuators operated in steady mode exhibit a characteristic wall jet behavior with peak velocity located approximately 1.4 mm above the wall. Although the near-wall peak velocity exhibits some increase with the number of actuators in the array, the primary effect of multiple actuators is a thickening of the wall jet and a corresponding increase in momentum flux. Within experimental uncertainty, the integrated momentum flux is found to be approximately independent of the distance from the actuator. Direct measurement of actuator thrust was found to be always less than that inferred from integrated momentum flux; this may be due to the neglect of end effects or a wall jet density that is below ambient.

Finally, it is noted that by using the results of this study, plasma flow control has been achieved in wind-tunnel tests of a full aircraft configuration. In particular, lift enhancement and drag reduction have been demonstrated at fuselage and wing Reynolds numbers of 6.8×10^6 and 1.2×10^6, respectively. In this manner, the results of the present study should serve to extend the applications of SDBD flow control to higher Reynolds number than previously achievable using Kapton-based plasma actuators.

Acknowledgments

This work was supported, in part, by Bell Helicopter and by NASA under Research Announcement NNX07AO09A. This financial support is gratefully acknowledged. The authors would also like to acknowledge Katie Thorne for her contributions to the serrated electrode study.

References

[1] Post, M. L., and Corke, T. C., "Separation Control on a High Angle of Attack Airfoil Using Plasma Actuators," *AIAA Journal*, Vol. 42, No. 11, 2004, pp. 2177–2184. doi:10.2514/1.2929

[2] Benard, N., Braud, P., and Jolibois, J., "Airflow Reattachment Along a NACA 0015 Airfoil by Surface SDBD Actuator-Time Resolved PIV Investigation," AIAA Paper 2008-4202, 2008.

[3] Post, M. L., and Corke, T. C., "Separation Control Using Plasma Actuators—Dynamic Stall Vortex Control on an Oscillating Airfoil," *AIAA Journal*, Vol. 44, No. 12, 2006, pp. 3125–3135. doi:10.2514/1.22716

[4] Do, H., Kim, W., Mungal, M. O., and Cappelli, M. A., "Bluff Body Flow Separation Control Using Surface Dielectric Barrier Discharges," AIAA Paper 2007-939, 2007.

[5] Thomas, F. O., Kozlov, A., and Corke, T. C., "Plasma Actuators for Cylinder Flow Control and Noise Reduction," *AIAA Journal*, Vol. 46, No. 8, 2008, pp. 1921–1931. doi:10.2514/1.27821

[6] Thomas, F. O., Kozlov, A., and Corke, T. C., "Plasma Actuators for Landing Gear Noise Control," AIAA Paper 2005-3010, 2005.

[7] Rizzetta, D., and Visbal, M., "Large-Eddy Simulation of Plasma-Based Control Strategies for Bluff Body Flow," AIAA Paper 2008-4197, 2008.

[8] Gregory, J., Porter, C., Sherman, D., and McLaughlin, T., "Circular Cylinder Wake Control Using Spatially Distributed Plasma Forcing," AIAA Paper 2008-4198, 2008.

[9] Schatzman, D., and Thomas, F. O., "Turbulent Boundary Layer Separation Control Using Plasma Actuators," AIAA Paper 2008-4199, 2008.

[10] Baughn, J. W., Porter, C., Peterson, B. L., McLaughlin, T. E., Enloe, C. L., Font, G. I., and Baird, C., "Momentum Transfer for an Aerodynamic Plasma Actuator with an Imposed Boundary Layer," AIAA Paper 2006-168, 2006.

[11] Font, G. I., "Boundary Layer Control with Atmospheric Plasma Discharges," *AIAA Journal*, Vol. 44, No. 7, 2006, pp. 1572–1578. doi:10.2514/1.18542

[12] Corke, T. C., He, C., and Patel, M., "Plasma Flaps and Slats: An Application of Weakly-Ionized Plasma Actuators," AIAA Paper 2004-2127, 2004.

[13] Huang, J., Corke, T. C., and Thomas, F. O., "Plasma Actuators for Separation Control of Low-Pressure Turbine Blades," *AIAA Journal*, Vol. 44, No. 1, 2006, pp. 51–57. doi:10.2514/1.2903

[14] Huang, J., Corke, T. C., and Thomas, F. O., "Unsteady Plasma Actuators for Separation Control of Low-Pressure Turbine Blades," *AIAA Journal*, Vol. 44, No. 7, 2006, pp. 1477–1487. doi:10.2514/1.19243

[15] Van Ness, D. K., II, Corke, T. C., and Morris, S. C., "Turbine Tip Clearance Flow Control Using Plasma Actuators," AIAA Paper 2006-0021, 2006.

[16] Fridman, A., and Kennedy, L. A., *Plasma Physics and Engineering*, Taylor and Francis, New York, 2004.

[17] Enloe, C. L., McLaughlin, T. E., VanDyken, R. D., Kachner, K. D., Jumper, E. J., Corke, T. C., Post, M., and Haddad, O., "Mechanisms and Responses of a Single Dielectric Barrier Plasma Actuator: Geometric Effects," *AIAA Journal*, Vol. 42, No. 3, 2004, pp. 595–604. doi:10.2514/1.3884

[18] Enloe, C. L., McLaughlin, T. E., VanDyken, R. D., Kachner, K. D., Jumper, E. J., Corke, T. C., "Mechanisms and Responses of a Single Dielectric Barrier Plasma Actuator: Plasma Morphology," *AIAA Journal*, Vol. 42, No. 3, 2004, pp. 589–594. doi:10.2514/1.2305

[19] Gibalov, V. I., and Pietsch, G. J., "The Development of Dielectric Barrier Discharges in Gas Gaps and on Surfaces," *Journal of Physics D: Applied Physics*, Vol. 33, No. 20, 2000, pp. 2618–2636. doi:10.1088/0022-3727/33/20/315

[20] Massines, F., Rabehi, A., Decomps, P., Ben Gadri, R., Segur, P., and Mayoux, C., "Experimental and Theoretical Study of a Glow Discharge

at Atmospheric Pressure Controlled by Dielectric Barrier," *Journal of Applied Physics*, Vol. 83, No. 6, 1998, pp. 2950–2957. doi:10.1063/1.367051

[21] Shyy, W., Jarayaman, B., and Anderson, A., "Modeling of Glow Discharge-Induced Fluid Dynamics," *Journal of Applied Physics*, Vol. 92, No. 11, 2002, pp. 6434–6443. doi:10.1063/1.1515103

[22] Singh, K. P., and Roy, S., "Modeling Plasma Actuators with Air Chemistry for Effective Flow Control," *Journal of Applied Physics*, Vol. 101, No. 12, 2007, pp. 123308-1–8.

[23] Jayaraman, B., Thakur, S., and Shyy, W., "Modeling of Fluid Dynamics and Heat Transfer Induced by Dielectric Barrier Plasma Actuator," *Journal of Heat Transfer*, Vol. 129, No. 4, 2007, pp. 517–525. doi:10.1115/1.2709659

[24] Suzen, Y. B., Huang, P. G., Jacob, J. D., and Ashipis, D. E., "Numerical Simulation of Plasma Based Flow Control Applications," AIAA Paper 2005-4633, 2005.

[25] Orlov, D. M., Corke, T. C., and Patel, M. P., "Electric Circuit Model for Aerodynamic Plasma Actuator," AIAA Paper 2006-1206, 2006.

[26] Moreau, E., "Airflow Control by Non-Thermal Plasma Actuators," *Journal of Physics D: Applied Physics*, Vol. 40, No. 3, 2007, pp. 605–636. doi:10.1088/0022-3727/40/3/S01

[27] Corke, T. C., Post, M. L., and Orlov, D. M., "SDBD Plasma Enhanced Aerodynamics: Concepts, Optimization and Applications," *Progress in Aerospace Sciences*, Vol. 43, Nos. 7–8, 2007, pp. 193–217. doi:10.1016/j.paerosci.2007.06.001

[28] Takashi, A., Yuji, T., and Syunichi, S., "A Parametric Experimental Study for Momentum Transfer by Plasma Actuator," AIAA Paper 2007-187, 2007.

[29] Forte, M., Jolibois, J., Moreua, F., Touchard, G., and Cazalens, M., "Optimization of a Dielectric Barrier Discharge Actuator by Stationary and Non-Stationary Measurements of the Induced Flow Velocity-Application to Flow Control," AIAA Paper 2006-2863, 2006.

[30] Dunn, P. F., *Measurement and Data Analysis for Engineering and Science*, McGraw-Hill, New York, 2005.

E. Livne
Associate Editor